Proceedings of the Zakopane School of Physics 2023 International Symposium, Zakopane, Poland, May 23–27, 2023

Controlling the Magnetic Properties of Fe-Based Composite Nanoparticles

O. Polit, M.S. Shakeri, Z. Swiatkowska-Warkocka*

Institute of Nuclear Physics Polish Academy of Sciences, Radzikowskiego 152, 31-342 Kraków, Poland

Doi: 10.12693/APhysPolA.145.139 *e-mail: zaneta.swiatkowska@ifj.edu.pl

We present Fe_xO_y composite particles prepared by pulsed laser irradiation of α-Fe_2O_3 nanoparticles dispersed in ethyl acetate and irradiated using a laser beam in the ultraviolet range with a wavelength of 355 nm. The sizes of particles and composition were controlled by tuning the laser parameters, such as laser fluence and irradiation time. We showed the evolution of the composition through X-ray diffraction measurements. Reactive bond molecular dynamics simulation results show bond breaking/formation during the synthesizing process. We examined the magnetic properties of the particles and showed that coercivity can be changed by the composition of particles and by increasing or decreasing particle size. The choice of systems built of iron and iron oxides made it possible to introduce the exchange bias effect into a range of magnetic properties of synthesized particles.

topics: composite particles, laser synthesis, molecular dynamics, magnetic properties

1. Introduction

Iron-based particles have unique magnetic, optical, electrical, and catalytic characteristics, making them suitable for a wide range of applications, including environmental remediation, catalysis, sensors, and diagnosis of diseases and therapy [1–3].

The physical properties of various iron oxide (Fe_xO_y) compounds can be extremely different, e.g., magnetite (Fe_3O_4) and magnemite (γ-Fe_2O_3) have been commonly used in biomedicine because their saturation magnetization is the highest [4]. The bandgap of hematite (α-Fe_2O_3) is from 2.0 to 2.2 eV, making it useful in applications that involve visible light absorption [5, 6]. Magnetite has unique electric and magnetic properties because its intrinsic crystal structure allows electrons to be transferred between Fe^{2+} and Fe^{3+} in the octahedral sites [7]. Fe_3O_4, γ-Fe_2O_3, and α-Fe_2O_3, including those in the form of the oxidized zerovalent iron core–shell structure, are widely used in heterogeneous catalysis processes and have been used as attractive alternatives for the treatment of wastewaters and soils contaminated with organic compounds [8–10]. The combination of these elements in one particle can result in a material with new or enhanced properties and broader applications. It is well known that the magnetic properties of iron-oxide particles depend on the particles' size, shape, and composition [11]. As the size reduces, below a certain value, the iron-oxide particles change from ferrimagnet/ferromagnet to superparamagnet [12]. Moreover, not only the chemical phase composition of composite particles, but also structural organization (e.g., random clusters of one phase in the other or core–shell structure) influence the magnetic properties [13].

The ability to control magnetic properties, such as saturation magnetization, remanent magnetization, and coercivity of these hybrids is important not only for the fundamental understanding of magnetism in these important materials, but also for their applications.

In the last decades, laser processing has become an important route for producing nanoparticles. The pulsed laser ablation method (PLA) uses a focused laser beam that can provide high energy density on small areas on target, leading to rapid growth of explosive nanoparticles [14–19]. Using an unfocused laser beam of moderate fluence to irradiate nanoparticles dispersed in a liquid medium results in a slightly different phenomenon. The irradiated material melts and subsequently merges to form submicrometer-sized spherical particles. The latter technique, referred to as pulsed laser irradiation in liquids (PLIL), proved to be a comprehensive and promising method for the synthesis of colloidal submicrometer spheres with outstanding properties [20–31]. So far, it has been shown to be an effective approach for the synthesis and control of a variety of composite particles with various morphology (core–shell, alloy) and compositions, which are not only metals or oxides, but also non-equilibrium bimetallic alloys (AuFe, AuCo, and AuNi). The size, morphology, and composition of obtained particles can be tuned in a controllable

manner by experimental parameters, such as wavelength, laser fluence, irradiation time, solvent, and molar ratio of irradiated materials [20]. This paper complements earlier reports on the irradiation of α-Fe_2O_3 nanoparticles dispersed in ethyl acetate [21] by investigating the effects of irradiation using a laser beam in the ultraviolet range with a wavelength of 355 nm (3rd harmonics). By changing the laser fluence and irradiation time, α-Fe_2O_3 is reduced to Fe_3O_4, FeO, and Fe. We show that by varying the laser parameters (laser fluence and/or irradiation time), we can control the phase composition of obtained particles, and thus, we can control the coercivity of obtained particles.

2. Materials and methods

2.1. Nanoparticles synthesis

Typically, raw nanoparticles of α-Fe_2O_3 (Sigma-Aldrich, average size $<$ 50 nm, 0.5 mM) were dispersed in ethyl acetate (5 ml). The resulting suspension was ultrasound-mixed and transferred to a sealed cell equipped with a quartz window. Then, the mixture was irradiated with an unfocused pulsed laser beam generated by Nd:YAG laser operating in the third harmonic mode at 355 nm wavelength and with a 30 Hz repetition rate. First, with fixed irradiation time (1 h), energy densities were changed in the range of 33–166 mJ/pulse cm^2. Then, with a fixed energy of 166 mJ/pulse cm^2, the time was varied in the 15–180 min range. During irradiation, an ultrasonic stirring was maintained to prevent sedimentation and gravitational settling of the suspension. Samples prepared by irradiation in laser fluence 166 mJ/pulse cm^2 were dried and heated in the air at 600°C for 1 h.

2.2. Characterization

The morphology of the obtained particles was observed by a field emission scanning electron microscope (FE-SEM; Hitachi S4800). The average particle size was determined by measuring the diameters of 200 particles from each SEM image. The crystal structure of particles was determined with an X-ray diffractometer (XRD; Rigaku Ultima IV) using standard θ–2θ geometry. The detection was performed using the Cu K_α (λ = 1.54 Å) radiation at operating current and voltage of 30 mA and 40 kV, respectively. All diffraction patterns were collected with a step size of 0.05° in the 2θ range from 20 to 80°. A highly sensitive superconducting quantum interference device (SQUID; Quantum Design, MPMS) magnetometer was employed to measure the magnetic properties of nanocomposite particles. Hysteresis measurements were recorded for dried samples of nanoparticles in a gelatin capsule. Hysteresis loops were obtained by using a maximum applied field up to 50 kOe at 5 K and 300 K. The exchange bias properties of samples were investigated by measuring field-cooled (FC) hysteresis loops in the temperature range of 5–300 K. In the FC procedure, the sample was cooled down from the initial temperature of 300 K to the measuring temperature T, under an applied field of 50 kOe. Once T was reached, the field was set to 50 kOe, and the measurement of the loop started. FullProf software was used for peak fitting and to evaluate the lattice constants of the material and quantitative phase analysis [32].

2.3. Modeling and simulation procedure

Using the ReaxFF module of the Amsterdam Modeling Suite (AMS) software package [33], molecular dynamics simulations (MD) were conducted using a reactive bond force field (RBFF) with Fe/C/H/O parameters [34]. A three-dimensional system with a parallelogram-shaped simulation box is constructed with periodic boundary conditions in all directions. There were four atomic layers in the Fe_2O_3 slab, each containing 200 iron and 300 oxygen atoms, arranged in a (111) direction. The slab was placed in the center of a 50 Å high box that held 180 solvent molecules (density 0.45 g/mL). The density is kept at less than half of the actual (real) density to avoid any errors in the molecular modeling. The canonical ensemble (NVT) and the Nosé–Hoover thermostat are used for MD simulation, with a damping constant of 100 fs. Prior to the RBFF simulations, the initial geometric configuration was optimized through energy minimization using the conjugate gradient algorithm. Then, the system was NVT-equilibrated at 298 K for 5 ps. Once the system has reached equilibrium, an RBFF-MD simulation is performed on it. In order to overcome the computational constraints, high temperatures are commonly employed in RBFF-MD simulations to accelerate reactions [35–37]. ReaxFF MD has been shown to work well for high-temperature simulations with a time step of 0.25 fs [35]. Every 100 frames (25 fs), the dynamic trajectory and binding data are captured. To identify the molecules that form during the simulation, a cut-off value of 0.3 is selected for the bond order in the species analysis. To cover all reactions, including those involving very short-lived species, a low cut-off value is useful. For the simulation box, three simulations were performed, and the average of these simulations was used for additional molecule formation/dissociation analysis. An AMS GPU was used to visualize the results of the simulation.

3. Results and discussion

In Fig. 1b–e, we can clearly see the increase in particle size from 30 to 650 nm with the increase in laser fluence from 66 to 166 mJ/pulse cm^2. On the

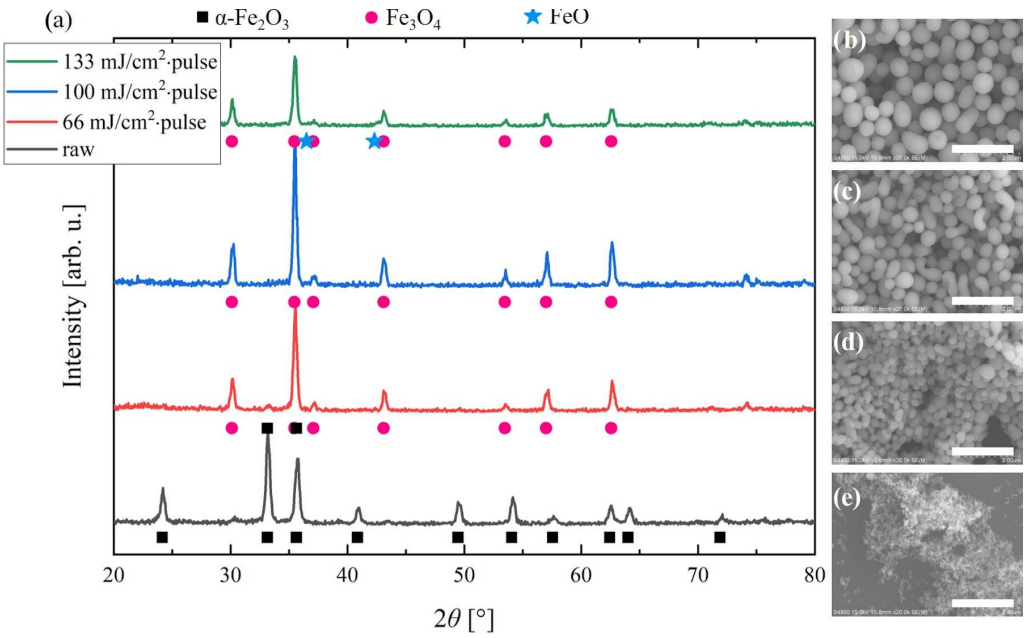

Fig. 1. (a) XRD results and (b–e) SEM images of raw α-Fe_2O_3 nanoparticles and particles obtained by pulsed laser irradiation (355 nm, 1 h) of α-Fe_2O_3 nanoparticles dispersed in ethyl acetate with various laser fluences: (b) 133 mJ/cm^{2}pulse, (c) 100 mJ/cm^{2}pulse, and (d) 66 mJ/cm^{2}pulse; (e) raw Fe2O3 nanoparticles. Scale bar on SEM images is 2 μm.

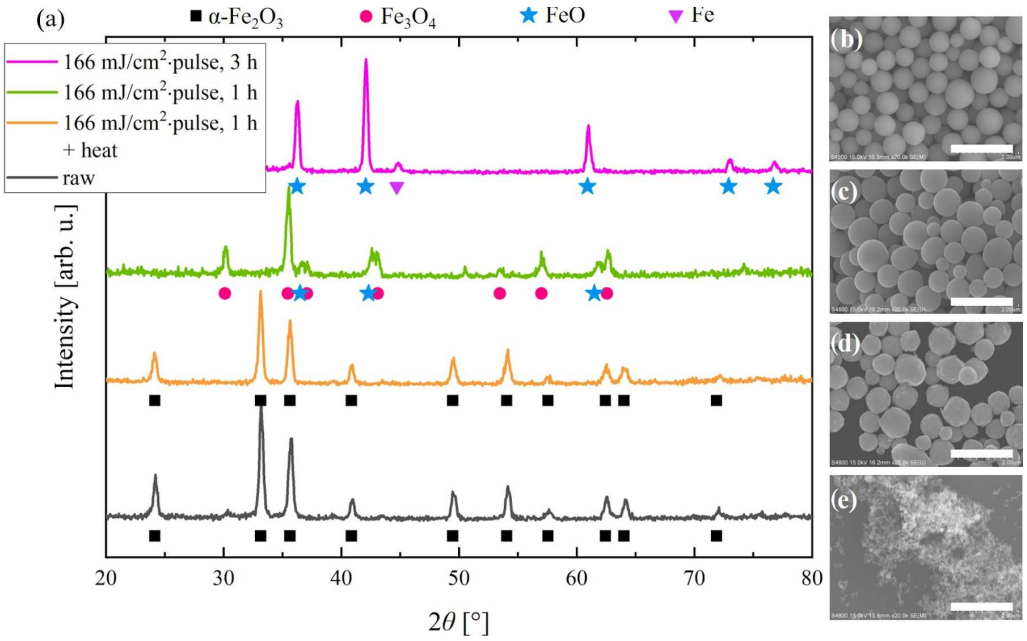

Fig. 2. (a) XRD results and (b–e) SEM images of raw α-Fe_2O_3 nanoparticles and particles obtained by pulsed laser irradiation (355 nm) of α-Fe_2O_3 nanoparticles dispersed in ethyl acetate with various irradiation times: (c) 1 h and (b) 3 h and, (d) after additional temperature treatment (600°C for 1 h) of particles from (c); (e) raw Fe_2O_3 nanoparticles. Scale bar on SEM images is 2 μm.

other hand, extending the exposure time to 3 h with a fixed energy fluence of 166 mJ/pulse cm^2 does not result in an increase in particle size (Fig. 2b–c). The structural transformation of hematite α-Fe_2O_3 to magnetite Fe_3O_4, wustite FeO, and iron Fe as a function of the laser irradiation parameters (fluence, time) has been observed by the XRD method (Figs. 1a, 2a). The raw nanoparticle diffractogram exhibits the diffraction peaks that correspond to crystal planes of hexagonal α-Fe_2O_3 (JCPDS card No. 80-2377) (R-3c). After irradiation with 66 mJ/pulse cm^2, the main phase of

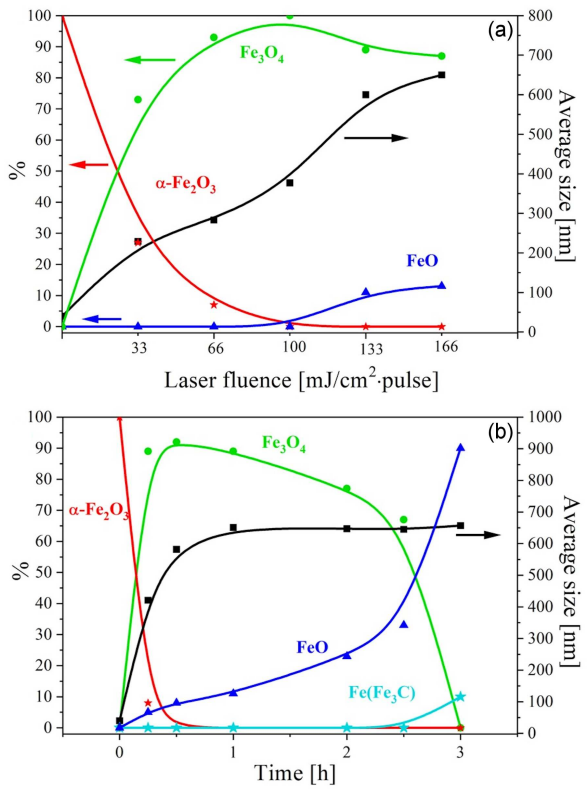

Fig. 3. (a) Dependence of particle size and phase changes on the laser fluence (1 h of irradiation). (b) Dependence of particle size and phase changes on irradiation time (166 mJ/pulse cm^2 fluence).

obtained particles is cubic Fe_3O_4 (JCPDS card No. 88-0315) (Fm-3m), but the diffraction peaks of α-Fe_2O_3 (33.2°, 35.6°) are also observed. The weight ratio of α-Fe_2O_3/Fe_3O_4, calculated from XRD data, is 7:93. As shown in Fig. 1a, the diffraction of particles irradiated with 100 mJ/pulse cm^2 peaks are indexed to the spinel structure, known for the Fe_3O_4 crystal, and no other peaks are detected, indicating that the product is pure phase Fe_3O_4.

A further increase in the laser fluence to 133 mJ/pulse cm^2 (Fig. 1a) and 166 mJ/pulse cm^2 (Fig. 2a) led to a complete reduction of hematite manifested by the disappearance of corresponding peaks, while the peaks of Fe_3O_4 at positions of 37.18°, 43.19°, and 62.56° are asymmetric. The careful analysis of the peak profiles indicated the presence of cubic FeO (JCPDS card No. 46–1312) (space group Fm-3m) phase. The amount of FeO phase in Fe_3O_4/FeO composites is 11% and 13% for 133 mJ/pulse cm^2 and 166 mJ/pulse cm^2, respectively. An increase in the irradiation time to 3 h results in a complete reduction of Fe_3O_4 to FeO and Fe (JCPDS card No. 85-1410), with a FeO/Fe weight ratio of 90:10. The XRD result shows that an hour of heating in air at a temperature of 600°C leads to complete oxidation of particles to α-Fe_2O_3 phase. As can be seen in Fig. 3, the size of particles increases gradually with an increase in laser fluence. For low laser fluence (up to 66 mJ/pulse cm^2), partial reduction of hematite to magnetite occurs. A further increase in laser fluence (100 mJ/pulse cm^2) leads to the complete reduction of hematite and the formation of magnetite. Then (for fluence 133 and 166 mJ/pulse cm^2), the transformation of magnetite into wustite is observed. To gain insight into the changes in the composition of nanoparticles during irradiation, we irradiated them with a laser fluence of 166 mJ/pulse cm^2 as a function of irradiation time. Compared to the irradiation of hematite with a wavelength of 532 nm (2nd harmonics) [21], higher energy was needed to obtain particles of similar sizes and composition, i.e., 180 mJ gave magnetite particles with a size of 600 nm, while in the case of the 3rd harmonic, 100 mJ was sufficient for the complete reduction of hematite to magnetite and obtaining particles with dimensions of 650 nm. Figure 3 shows changes in both particle size and composition for irradiation times ranging from 15 to 180 min. During the first hour, the size increases rapidly and then saturates at a diameter of approximately 600 nm. A similar trend was observed during NiO irradiation (532 nm, 10 Hz, 130 mJ/pulse cm^2) and reported in our previous work [28]. Here, half an hour is sufficient for a complete reduction of hematite, and further extension of the exposure time causes a gradual reduction of magnetite to FeO. Only after three hours does decomposition to Fe occur.

Phase diagrams calculated as the dependence of particle size on the required laser fluence J for Fe_2O_3 systems explain the differences in the results obtained at two different wavelengths. In the case of the 2nd harmonic, as shown in previous work [21], the laser fluence has a minimum value of 200 mJ/pulse cm^2 for particles with a diameter of about 200 nm. The calculations shown in Fig. 4 clearly show that in the case of the 3rd harmonic, the minimum laser fluence is 25 mJ/pulse cm^2. The calculations presented in Fig. 4 clearly show that a laser fluence of 33 mJ/pulse cm^2 is sufficient to decompose hematite particles up to 100 nm in size into magnetite, but not sufficient to melt these particles. It is known that nanoparticles form agglomerates and this fact influences the particle formation process. If agglomerates are larger than 100 nm, the energy needed to decompose hematite and melt the particles has to be higher.

A big role is played here by the interaction between the solvent and the solid phase, started by the absorption of ethyl acetate on the solid surface [22]. Figure 5a, b shows the top and three-dimensional side views of the simulation model. Based on the temperature and energy of the RBMD simulation, the interaction between the solvent and the solid phase is started by the absorption of a solvent molecule at the solid surface. The final products of the process, if the solvent has enough time to fully dissociate, are H_2O and CO_2, as expected. Smaller hydrocarbon species rise to a certain point

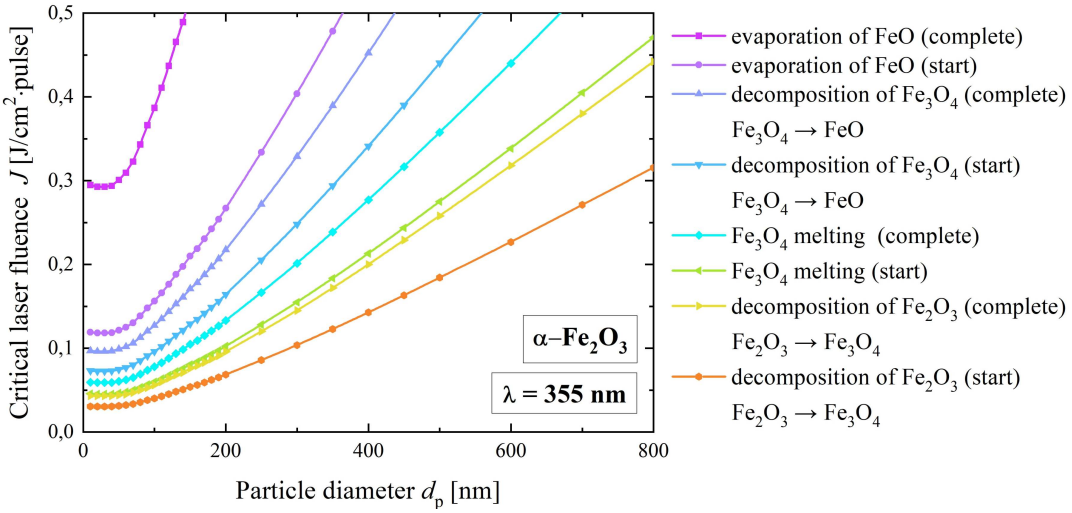

Fig. 4. Phase diagram calculated as particle size dependence of the required laser fluence for Fe_2O_3 systems to heat a particle to the decomposition, melting point, complete melting, boiling point, and complete evaporation using 355 nm laser. Detailed descriptions corresponding to line colors are provided in the chart legend.

in the reaction and then fall as the other species form; this process continues until the final products, i.e., carbon dioxide and water are obtained (Fig. 5d).

The breakdown of solvent is started by the absorption of the separated OH groups on the surface. After the remaining C_2H_5 decomposes to form C_2H_4, smaller hydrocarbons are produced (Fig. 5d). Time-dependent snapshots of the MB1 cross-section show the separation of iron atoms/clusters compounds into the solvent, whereas the solvent-dissociated molecules tend to remain on the slab's surface layers in an attempt to continue the separation process (Fig. 5e, f). The dissociated species diffuse into the Fe-oxide sphere, where the reduction reactions take place.

For magnetic measurements, we chose four samples, two with the same composition (α-Fe_2O_3) but different sizes, 30 and 650 nm (Fig. 6a, b), and two with submicrometer sizes but different compositions, α-Fe_2O_3/Fe_3O_4 and FeO/Fe (Fig. 6c, d). We measured the magnetic hysteresis loop at two temperatures, 5 K and 300 K. The loops at 5 K were measured after cooling the sample in the presence of an external magnetic field of 50 kOe. Figure 6a shows magnetic measurements for raw hematite α-Fe_2O_3 with an average size of around 30 nm. In both temperatures, the hysteresis exhibits a ferromagnetic type of behavior, and a coercive field at 5 K is visibly larger than at 300 K, which is to be expected in this kind of system [38, 39]. Figure 6b shows a hysteresis loop for composite particles obtained through irradiation of α-Fe_2O_3 nanoparticles dispersed in ethyl acetate and irradiated with a laser fluence of 166 mJ/pulse cm^2 for 3 h, after which the sample was heated to 600°C for 1 h. During irradiation, we created submicrometer particles with an average size of around 650 nm, composed of reduced

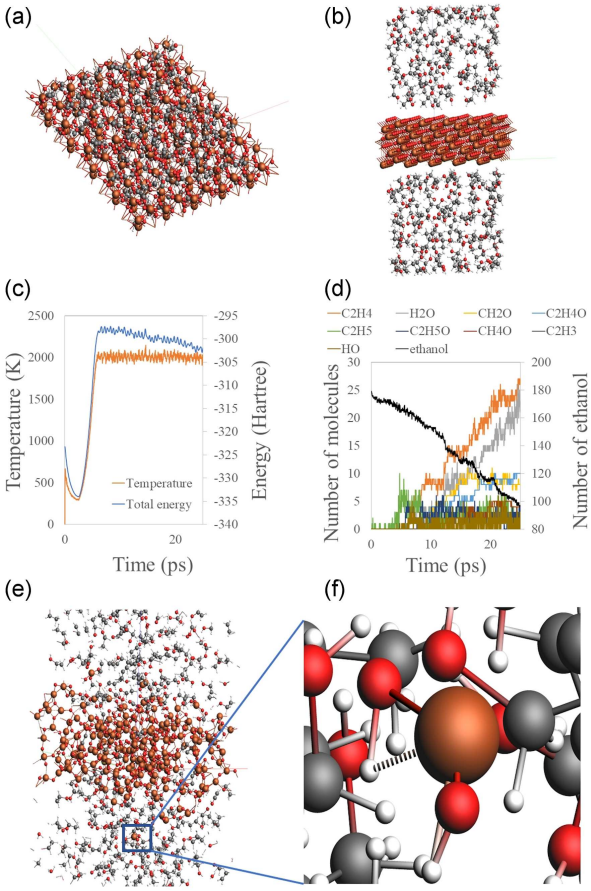

Fig. 5. Molecular dynamics simulations results: (a) front and (b) side views of molecular dynamics model, (c) temperature and energy changes vs time steps of simulation, (d) solvent dissociation and formation of smaller species, (e) snap-shot of simulation box after finishing the calculations, (f) iron atom bonding inside the solvent bath.

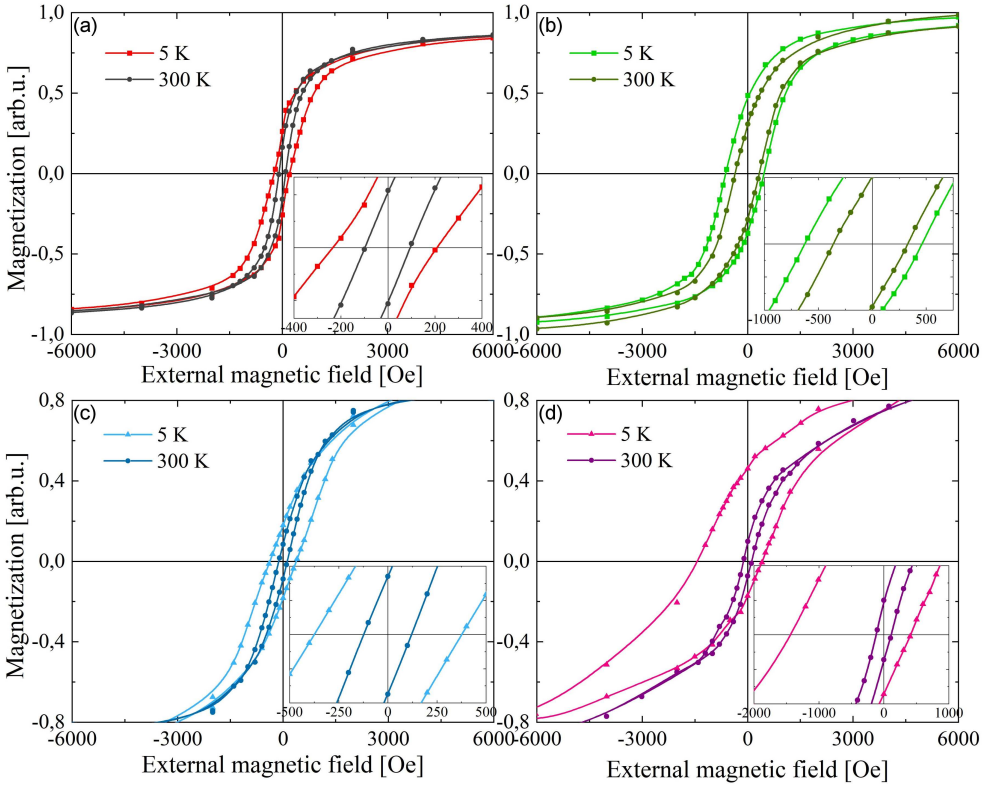

Fig. 6. Magnetic hysteresis loops measured at two temperatures of 5 K and 300 K for systems: (a) raw α-Fe_2O_3, (b) α-Fe_2O_3 irradiated with laser fluence of 166 mJ/pulse cm^2 and heated at 600°C for 1 h, (c) α-Fe_2O_3 irradiated with fluence of 66 mJ/pulse cm^2 for 1 h, (d) α-Fe_2O_3 irradiated with fluence of 166 mJ/pulse cm^2 for 3 h. Every chart contains an inset with a part of the hysteresis loop that was magnified around the center of the coordinate system to make characteristic points of hysteresis more visible.

iron oxides, i.e., FeO and Fe_3O_4. After heating these particles, almost the entire sample oxidized back to hematite, so we obtained the same component as raw material with a changed diameter of particles. The magnetic hysteresis loop for this sample shows the increased value of coercivity both for 5 K and 300 K. At 5 K, the coercive field is 215 Oe and 545 Oe for raw nanoparticles and irradiated particles, respectively. Near room temperature coercivity is also significantly increased, to 100 Oe for nanoparticles and 340 Oe for submicrometer particles. There are many studies in the literature on the magnetic properties of hematite, where significant differences in coercivity values are observed [40–43]. It has been shown that factors such as particle size, shape, morphology, dipolar and exchange interactions, defects, and microstructure of hematite particles have a huge impact on the coercivity value. The coercivity of nanoparticles in 300 K is similar to that reported by other researchers [40, 41]. The increase in coercivity for submicron particles, which can be explained by the assembly of the small and oriented particles into the superstructures, results in the change of the single domain to the multidomain, leading to higher remanent magnetization and coercivity [41, 42]. It has been reported that the crystallographic arrangement of grains and the boundaries between them contribute to high coercivity [43]. High coercivity may also result from magnetoelastic anisotropy caused by internal deformations in small particles and defects in large crystals [40].

Figure 6c shows results for the system obtained through irradiation of α-Fe_2O_3 with a laser fluence of 66 mJ/pulse cm^2 for 1 h, while Fig. 6d shows measurements for particles obtained by irradiation of α-Fe_2O_3 with a fluence of 166 mJ/pulse cm^2 for 3 h. From XRD measurements, we know that the first sample is composed of Fe_3O_4 with a small amount of α-Fe_2O_3, and the second sample is composed of FeO and Fe. At room temperature, coercivity in both cases is almost the same — 110 Oe and 120 Oe for samples with shorter and longer times of irradiation, respectively. However, there are clear differences at low temperatures. The sample composed of α-Fe_2O_3/Fe_3O_4 has a coercive field of 380 Oe, while the sample composed of FeO/Fe has a coercivity of 955 Oe and exhibits a shift of hysteresis loop along an axis of the external magnetic field, which is a characteristic feature of exchange bias effect. Exchange bias is a phenomenon associated with interfacial interactions between ferromagnetic and antiferromagnetic materials. The shift of the center of the hysteresis loop is called the exchange

bias field H_{EX}. In our system, the shift is equal to 475 Oe and is very well visible in Fig. 6d. This specific sample is composed of Fe, which is ferromagnetic at room temperature, and FeO, which is antiferromagnetic below 198 K. In 300 K, FeO is in a paramagnetic state, and we cannot observe the exchange bias effect (Fig. 6d; purple curve) for this system. However, if we cool down the sample to low temperatures in the presence of an external magnetic field, we can observe a shift of the hysteresis loop and enlargement of the coercive field (Fig. 6d; pink curve). This phenomenon is caused by the coupling of magnetic moments between ferromagnet and antiferromagnet below the Néel temperature of FeO [44, 45]. We also observed this effect in other samples containing FeO and ferro-/ferrimagnetic iron oxides, e.g., Fe_3O_4, and the strength of the effect depends on the quantity of antiferromagnetic to ferro-/ferrimagnetic material [25]. Therefore, we can see that by varying parameters of the synthesis of composite particles during irradiation in a liquid process, we can strongly influence the magnetic properties of composites and even introduce additional effects to the system.

4. Conclusions

In conclusion, the pulsed laser irradiation technique has been demonstrated to be a simple method for obtaining submicron iron oxide-based heterostructure particles. We have shown that by changing the laser parameters (laser fluence and exposure time), we can control not only the amount but also the degree of reduction of α-Fe_2O_3 to Fe_3O_4, FeO, and finally to Fe. We have shown that by changing the size and composition of particles, we can change their magnetic properties. We believe that our research will help synthesize materials with specific properties for dedicated applications.

References

[1] L. Mohammed, H.G. Gomaa, D. Ragab, J. Zhu, *Particuology* **30**, 1 (2017).

[2] A.M. Diez-Pascual, *Polymers* **11**, 1790 (2019).

[3] A. Suhasini, K.P.V. Kumar, T. Maiyalagan, *Sci. Eng. Compos. Mater.* **25**, 189 (2018).

[4] I. Fatimah, G. Fadillah, S.P. Yudha, *Arab. J. Chem.* **14**, 103301 (2021).

[5] A. Kay, I. Cesar, M. Gratzel, *J. Am Chem Soc.* **128**, 15714 (2006).

[6] C. Karunakaran, P. Anilkumarl, *J. Mol. Catal. A Chem.* **265**, 153 (2007).

[7] B.Y.Geng, J.Z. Ma, J.H. You, *Cryst. Growth Des.* **8**, 1443 (2008).

[8] M.C. Pereira, L.C.A. Oliveira, E. Murad, *Clay Miner.* **47**, 285 (2012).

[9] S.R.R. Pouran, A.A.A. Raman, W.M.A.W. Daud, *J. Clean. Prod.* **64**, 24 (2014).

[10] Y. Mu, F. Jia, Z. Ai, L. Zhang, *Environ. Sci. Nano* **4**, 27 (2017).

[11] C. Montferrand, L. Hu, I. Milosevic, V. Russier, D. Bonnin, L. Motte, A. Brioude, Y. Lalatonne, *Acta Biomater.* **9**, 6150 (2013).

[12] M. Busquets, A. Espargaró, R. Sabaté, J. Estelrich, *Nanomaterials* **5**, 2231 (2015).

[13] A.G. Kolhatkar, A.C. Jamison, D. Litvinov, R.C. Willson, T.R. Lee, *Int. J. Mol. Sci.* **14**, 15977 (2013).

[14] F. Mafune, J. Kohno, Y. Takeda, T. Kondow, H. Sawabe, *J. Phys. Chem. B* **104**, 9111 (2000).

[15] V. Amendola et al., *Nanoscale* **5**, 5611 (2013).

[16] J. Jakobi et al., *Nanotechnology* **22**, 145601 (2011).

[17] E. Gordon, A. Karabulin, V. Matyushenko, V. Sizov, I. Khodos, *Phys. Chem. Chem. Phys.* **16**, 25229 (2014).

[18] K.D. Malviya, K. Chattopadhyay, *J. Phys. Chem. C* **118**, 13228 (2014).

[19] V. Amendola, S. Scaramuzza, S. Agnoli, S. Polizzi, M. Meneghetti, *Nanoscale* **6**, 1423 (2014).

[20] Y. Ishikawa, T. Tsuji, S. Sakaki, N. Koshizaki, *Prog. Mater. Sci.* **131**, 101004 (2023).

[21] M.S. Shakeri, O. Polit, B. Grabowska-Polanowska, A. Pyatenko, K. Suchanek, M. Dulski, J. Gurgul, Z. Swiatkowska-Warkocka, *Sci. Rep.* **12**, 11950 (2022).

[22] M. Sadegh Shakeri, Z. Swiatkowska-Warkocka, O. Polit et al., *Adv. Funct. Mater* **33**, 2304359 (2023).

[23] H. Wang, L. Jia, L. Li, X.X. Li, Z. Swiatkowska-Warkocka, K. Kawaguchi, A. Pyatenko, N. Koshizaki, *J. Mater. Chem. A* **1**, 692 (2013).

[24] H. Wang, N. Koshizaki, L. Li, L. Jia, K. Kawaguchi, X. Li, A. Pyatenko, Z. Swiatkowska-Warkocka, Y. Bando, D. Golberg, *Adv. Mater.* **23**, 1865 (2011).

[25] Z. Swiatkowska-Warkocka, K. Kawaguchi, H.Q. Wang, Y. Katou, N. Koshizaki, *Nanoscale Res. Lett.* **6**, 226 (2011).

[26] H.Q. Wang, A. Pyatenko, K. Kawaguchi, X.Y. Li, Z. Swiatkowska-Warkocka, N. Koshizaki, *Angew. Chem., Int. Ed* **49**, 6361 (2010).

[27] H. Wang, K. Kawaguchi, A. Pyatenko, X. Li, Z. Swiatkowska-Warkocka, Y. Katou, N. Koshizaki, *Chem. Eur. J.* **18**, 163 (2012).

[28] Z. Swiatkowska-Warkocka, A. Pyatenko, Y. Shimizu, M. Perzanowski, A. Zarzycki, B.R. Jany, M. Marszalek, *Nanomaterials* **8**, 790 (2018).

[29] Z. Swiatkowska-Warkocka, A. Pyatenko, F. Krok, B.R. Jany, M. Marszalek, *Sci. Rep.* **5**, 09849 (2015).

[30] Z. Swiatkowska-Warkocka, A. Pyatenko, K. Koga, K. Kawaguchi, H. Wang, N. Koshizaki, *J. Phys. Chem. C* **121**, 8177 (2017).

[31] H. Fuse, N. Koshizaki, Y. Ishikawa, Z. Swiatkowska-Warkocka, *Nanomaterials* **9**, 198 (2019).

[32] Fullprof Software (accessed on 5 October 2023).

[33] R. Rüger, M. Franchini, T. Trnka, A. Yakovlev, E. van Lenthe, P. Philipsen, T. van Vuren, B. Klumpers, T. Soini, AMS 2022.1, SCM, Theoretical Chemistry, Vrije Universiteit, Amsterdam, The Netherlands.

[34] Ch. Zou, A. Van Duin, *JOM* **64**, 1426 (2012).

[35] K. Chenoweth, A.C.T. Van Duin, W.A. Goddard, *J. Phys. Chem. A* **112**, 1040 (2008).

[36] M. Feng, X.Z. Jiang, K.H. Luo, *Proc. Combust. Inst.* **37**, 5473 (2019).

[37] Q. Mao, A.C.T. Van Duin, K.H. Luo, *Carbon* **121**, 380 (2017).

[38] Ö. Özdemir , *Geophys. J. Int.* **141**, 351 (2000).

[39] I. Lyubutin, S. Lin, Y.V. Korzhetskiy, T.V. Dmitrieva, R.K. Chiang, *J. Appl. Phys.* **106**, 034311 (2009).

[40] M. Tadic, D. Trpkov, L. Kopanja, S. Vojnovic, M. Panjan, *J. Alloys Compd.* **792**, 599 (2019).

[41] J. Lian, X. Duan, J. Ma, P. Peng, T. Kim, W. Zheng, *ACS Nano* **3**, 3749 (2009).

[42] J. Ma, J. Lian, X. Duan, X. Liu, W. Zheng, *J. Phys. Chem. C* **114**, 10671 (2010).

[43] A.R. Goldman, E. Asenath-Smith, L.A. Estroff, *APL Mater.* **5**, 104901 (2017).

[44] M. Kiwi, *J. Magn. Magn. Mater.* **234**, 584 (2001).

[45] J. Nogués, I.K. Schuller, *J. Magn. Magn. Mater.* **192**, 203 (1999).